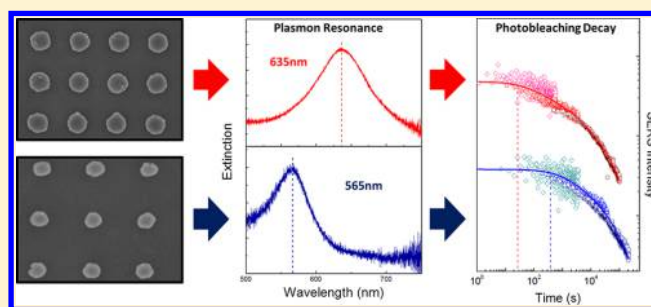


Photobleaching of Fluorophores on the Surface of Nanoantennas

C. M. Galloway,[†] C. Artur,[†] J. Grand,[‡] and E. C. Le Ru^{*,†}[†]The MacDiarmid Institute for Advanced Materials and Nanotechnology, School of Chemical and Physical Sciences, Victoria University of Wellington, PO Box 600 Wellington 6140, New Zealand[‡]Université Paris Diderot, Sorbonne Paris Cité, ITODYS, UMR CNRS 7086, 15 rue J-A de Baïf, 75205 Paris Cedex 13, France

S Supporting Information

ABSTRACT: Photobleaching is a widespread problem in any optical study or application involving fluorophores and is particularly acute in the context of single-molecule detection. Fluorophores adsorbed on metallic nanostructures are not immune to this problem, but little effort has been devoted to understanding how photobleaching is modified on metallic surfaces and if any additional mechanisms are involved. Here, we tackle this issue both theoretically and experimentally. We present a model accounting for the modification of the standard triplet-state-mediated photobleaching mechanism on metal nanostructures supporting plasmon resonances. The wide distribution of enhancement factors on the surface is shown to result in an extremely nonexponential decay with a range of decay rates covering several orders of magnitude. This model is verified experimentally by performing time-dependent and power-dependent surface-enhanced Raman and fluorescence measurements on uniform arrays of gold nanodiscs with tunable plasmon resonances. We, moreover, discuss the possibility of extracting the enhancement factor distribution from such experiments. Finally, additional mechanisms of photobleaching associated with photoinduced heating of the metallic nanostructures are shown to play a role in some conditions. This study of photobleaching on nanoantennas paves the way for developing new techniques to either mitigate the problems or further exploit them.



INTRODUCTION

Over the past decade or so, there has been a steady interest in exploiting the electromagnetic enhancements arising from plasmon resonances in metallic nanoantennas to boost the spectroscopic signals of fluorophores and other molecules; surface-enhanced fluorescence (SEF) and surface-enhanced Raman spectroscopy (SERS)¹ are the most prominent examples. Increasing efforts have also recently focused on exploiting metallic nanoparticles and plasmon resonances to enhance photochemical and photocatalytic reactions.^{2–5} The main emphasis in this case is on the use of hot electrons excited via the plasmon resonance, although electromagnetic enhancements may also play a role. At the crossroad between those two streams of research, one particular aspect of surface-enhanced spectroscopies that has been largely overlooked so far is how the metallic nanostructures modify the photobleaching (PB) properties of fluorophores. Related to this is the question of how such modifications may affect the performances of SERS or SEF-based techniques. Although photobleaching can be exploited for specific purposes,⁶ it is usually a significant concern in any form of fluorescence studies or applications (e.g., biotags), as it places a limit on the number of photons that can be collected from a single fluorescent molecule before the emission ceases. It is common knowledge that SERS and SEF are not immune to these photostability issues, as evidenced, for example, by the decay of the signals⁷ or by the appearance of the characteristic broad Raman peaks of

amorphous carbon.^{8–10} It has also been shown that these effects could have a dramatic impact on the apparent SERS enhancements¹¹ and, therefore, on any application of the technique. Even nonresonant molecules are affected by photostability issues,¹² although the mechanisms involved are expected to be different from those for fluorophores. Despite the fact that some of these effects were theoretically predicted more than 30 years ago¹³ and that isolated preliminary studies have been attempted,¹⁴ no dedicated experimental studies have so far been carried out to elucidate the mechanisms of PB of fluorophores near metallic nanostructures. Despite their obvious importance for any practical applications of SEF and SERS, simple questions have not yet been addressed in detail: Does a metallic nanoparticle improve or reduce the photostability of fluorophores? Does the local field enhancement affect the photostability and, if yes, by which amplitude and mechanism? The latter is especially important when considering the extreme (long-tail) nature of the EF distribution in all hot-spot-containing substrates.¹⁵ It would imply a similarly nonuniform and extreme distribution of PB decay rates, which would severely complicate any interpretations of SERS/SEF experiments with fluorophores. From a more positive point of view, a detailed understanding of the link between EF and PB

Received: October 6, 2014

Revised: November 19, 2014

Published: November 20, 2014

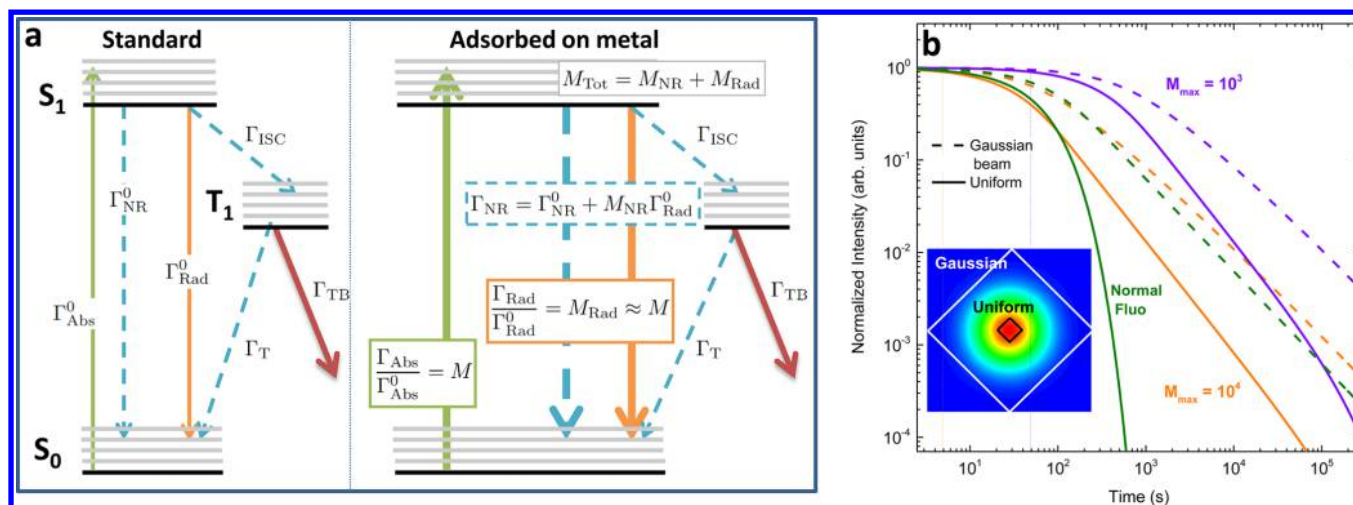


Figure 1. Theoretical predictions of photobleaching decay on nanoantennas. (a) Jablonski diagrams representing transitions (and associated rates Γ) involved in the fluorescence and photobleaching processes in standard conditions and for a fluorophore adsorbed on a metal surface. The dashed lines correspond to nonradiative transitions. (b) Predictions of the normalized intensity decays from eq 1 (normal fluorescence) and from eq 10 (SERS) for a truncated Pareto distribution of enhancement factors: $p(M) = 2AM^{-1-2k}$ for $M_{min} \leq M \leq M_{max}$. The parameters are set as $k = 0.4$, $M_{min} = 1$, and either $M_{max} = 10^3$ or 10^4 . The power density is $S_0 = 50 \text{ W cm}^{-2}$ and the PB parameters are taken as $\gamma_B^0 = 3.2 \times 10^{-4} \text{ s}^{-1} \text{ W}^{-1} \text{ cm}^2$ and $\alpha_B = 8 \times 10^{-8} \text{ s}^{-1} \text{ W}^{-1} \text{ cm}^2$. Both uniform excitation (solid lines) and Gaussian beam excitation (dashed lines) are considered.

rate would allow us to derive the full EF distribution from measurements of the PB dynamics, in the same spirit as the experiments in ref 12 using nonresonant molecules.

It is the aim of this study to tackle these outstanding questions. To do so, we provide a simple theoretical description of the modified PB properties where the enhancement factor distribution is explicitly factored in. This model is validated experimentally by studying the time dependence of the surface-enhanced resonance Raman scattering (SERRS) signal for the fluorophore Nile Blue (NB) adsorbed on the surface of arrays of gold nanodiscs. By varying the incident power densities, PB decay rates spanning 5 orders of magnitude are evidenced on a single substrate, providing strong experimental confirmation for the spread of the EF distribution and its close relationship with PB. We further discuss how some properties of the EF distribution, such as the maximum EF, can be extracted from the measured PB decay curves. Finally, an additional concomitant PB mechanism is evidenced for the largest power densities. Further experiments allow us to attribute this regime to a photoinduced temperature increase, highlighting the possible importance of thermal effects in the PB dynamics.

This study therefore provides a detailed theoretical and experimental investigation into the mechanisms of PB of fluorophores on metallic nanostructures supporting plasmon resonances. As such, it will provide a solid basis for further studies into new methods to mitigate PB effects and into alternative mechanisms of PB (for example, for nonresonant molecules) and how they relate to the EF distribution. Such an outcome would have a large impact not only on SERS/SEF research but also on applications of SEF in biology (e.g., for biomarkers), where the use of fluorophores and, therefore, the potential for photobleaching is unavoidable. Looking further afield, the understanding of the link between EF distributions and PB will also benefit recent efforts to exploit EM hot-spots for other types of photochemical reactions.^{3-5,16,17}

THEORETICAL FRAMEWORK

Despite its importance to SERS and SEF experiments, there has not been much discussion of theoretical models of PB for molecules on metal surfaces in the literature. Earlier works studied the modification of the rates of the relevant physical processes but did not consider the distribution of enhancement factors.^{13,18} More recently, the most detailed model was arguably discussed in the appendix of ref 19, but it considered only Gaussian profiles of enhancement factors. The effect of a general enhancement factor distribution is discussed in ref 15 and is further developed in ref 20. However, none of those works provide a physical explanation for the modification of the PB decay rate or account for the change in excited state decay rates.²¹ A model accounting for all decay rate modifications is presented in ref 1, but the effect of the enhancement factor distribution is ignored. In this section, we expand and combine all these steps into a complete quantitative model of PB on metal surfaces accounting for decay rate modifications, enhancement factor distribution, and nonuniform excitation. We will here rely on the established electromagnetic model of SERS^{1,22,23} and SEF,²⁴⁻²⁷ in particular recent developments in the study of nonradiative processes,^{21,28-30} and studies of enhancement factor distributions.^{12,15,31,32} Only the most relevant results that are needed to account for photobleaching effects will be recalled, and the reader is referred to the previous literature for further details on these models. We will also use the same notations as in previous studies.^{1,21,23,24,26,27,30}

Photobleaching in Standard Conditions. The exact mechanisms of PB of fluorophores can be very diverse and are arguably not fully elucidated.³³⁻³⁹ Nevertheless, it is commonly accepted that in most cases, irreversible photodestruction is mediated via a transition from the excited singlet state S_1 to the excited triplet state T_1 (so-called intersystem crossing or ISC), which causes it to be reactive with surrounding molecules.^{33,34,37,38} The key intermolecular interaction is between the triplet excited fluorophore and oxygen molecules as this can create oxygen radicals, which can then destroy the fluorophore.^{33,38} Consequently, the probability that a molecule

photobleaches is dependent on the time spent in the triplet state, the reactivity of the molecule, and the surrounding environment.⁴⁰

We here adopt the simplest ISC model capturing all relevant processes in the molecule, as shown schematically in Figure 1a. The PB quantum yield ϕ_B is the probability of destruction for a molecule in S_1 and is the product of the probabilities of ISC by that of irreversible bleaching while in T_1 . The rate of PB is then simply $\Gamma_B^0 = \Gamma_{\text{Abs}}^0 \phi_B^0$, where Γ_{Abs}^0 is the rate of photon absorption and is proportional to the incident laser power density S_L , that is, $\Gamma_{\text{Abs}}^0 = \sigma_{\text{Abs}}^0 S_L$, where σ_{Abs}^0 is the absorption cross section. It will be convenient to write $\Gamma_B^0 = \gamma_B^0 S_L$, where $\gamma_B^0 = \sigma_{\text{Abs}}^0 \phi_B^0$ is an intrinsic PB characteristic of the fluorophore and its interaction with the environment. For a collection of identical molecules, the fluorescence intensity can then be obtained as

$$I_{\text{Fluo}}(t, S_L) = \mu_m Q^0 \sigma_{\text{Abs}}^0 P_L \exp(-\gamma_B^0 S_L t) \quad (1)$$

where μ_m is the number of molecules per unit area, P_L is the laser power, and $Q^0 = \Gamma_{\text{Rad}}^0 / (\Gamma_{\text{Rad}}^0 + \Gamma_{\text{NR}}^0)$ is the fluorescence quantum yield, with Γ_{Rad}^0 and Γ_{NR}^0 the radiative and non-radiative decay rates.

The decay is therefore monoexponential with a rate proportional to the incident power density. Values for the relevant parameters in the case of the dye Nile Blue used in this study are provided in section S.I of the Supporting Information.

Photobleaching on Metallic Surfaces. On metallic surfaces, all the decay rates whose underlying physical cause is electromagnetic will be modified.¹ In particular, the absorption rate is enhanced by the so-called local field intensity EF M_{Loc} , the radiative decay rate is enhanced by a factor M_{Rad} , and there is a new nonradiative decay channel associated with nonradiative emission into the metal (i.e., emission of a photon absorbed by the metal) and whose rate is $\Gamma_{\text{NR}} = M_{\text{NR}} \Gamma_{\text{Rad}}^0$. The total modification of the excited state decay rate is therefore $M_{\text{Tot}} = M_{\text{Rad}} + M_{\text{NR}}$. M_{Tot} , M_{Rad} , and M_{NR} relate to the electromagnetic interaction of the fluorophore with the metal surface and are independent of its intrinsic nonradiative decay or quantum yield (which can be strongly fluorophore-dependent).^{21,26,30,41} Note that M_{Loc} and M_{Rad} are of the same order by virtue of optical reciprocity²³ and are typically in the range 10^2 – 10^4 . We will assume for simplicity that they are equal, and we denote $M = M_{\text{Loc}} \approx M_{\text{Rad}}$ in the following. M_{NR} is responsible for fluorescence quenching and can be larger for molecules directly adsorbed on the metal^{21,24,28} with typical values about 10^5 . M_{NR} is also strongly dependent on the distance d from the surface (as $1/d^3$ in a first approximation)^{21,28} and is responsible for the large variation in SEF intensity as a function of d .

There is some discussion in the literature regarding plasmon coupling from the triplet state,^{42,43} but any modification to the triplet lifetime is relatively minor. We can therefore assume that the other transitions are not affected by the metal surface in a first approximation, and the modified photophysical properties can therefore be expressed in terms of the nonmodified ones as follows:

$$\Gamma_{\text{Abs}} / \Gamma_{\text{Abs}}^0 = M \quad (2)$$

$$\phi_B / \phi_B^0 = \frac{1}{Q^0 M_{\text{Tot}} + 1 - Q^0} \approx \frac{1}{Q^0 M_{\text{Tot}}} \quad (3)$$

$$\gamma_B / \gamma_B^0 = \frac{M}{Q^0 M_{\text{Tot}} + 1 - Q^0} \approx \frac{M}{Q^0 M_{\text{Tot}}} \quad (4)$$

where the latter approximation is valid in most relevant cases.

Because of the reduction in excited state lifetime, the probability of ISC to T_1 is reduced accordingly. This results in a strongly decreased PB quantum yield (eq 3). This means that each molecule is able to emit on average many more photons before it photobleaches ($Q^0 M_{\text{Tot}} \approx 4000 \times$ more for Nile Blue if $M_{\text{Tot}} = 10^5$). In terms of the PB decay rate Γ_B , the decrease in ϕ_B is partly compensated by the increase by a factor M in the absorption rate (eq 4). Because $M_{\text{Tot}} \gg M$ for molecules directly adsorbed on the surface, one may nevertheless expect from eq 4 an overall reduction in the photobleaching decay rate for molecules on metal surfaces, at least when $Q^0 \approx 1$.

Both fluorescence (SEF) and Raman (SERS) signals are modified on the surface,^{1,21,24} and assuming $M_{\text{Rad}} \approx M^2$ and neglecting the Stokes shifts, the SEF and SERS enhancement factors are

$$M_{\text{SEF}} = \frac{M^2}{Q^0 M_{\text{Tot}} + 1 - Q^0} \approx \frac{M^2}{Q^0 M_{\text{Tot}}} \quad (5)$$

$$M_{\text{SERS}} = M^2 \quad (6)$$

For a collection of molecules experiencing the same enhancements and taking into account $M_{\text{Tot}} \gg (Q^0)^{-1}$, the time-dependent intensities are then

$$I_{\text{SEF}}(t, S_L) = \mu_m Q^0 \sigma_{\text{Abs}}^0 P_L \frac{M^2}{Q^0 M_{\text{Tot}}} \exp(-\alpha_B M S_L t) \quad (7)$$

$$I_{\text{SERS}}(t, S_L) = \mu_m \sigma_{\text{Raman}}^0 P_L M^2 \exp(-\alpha_B M S_L t) \quad (8)$$

where

$$\alpha_B = \gamma_B^0 / (Q^0 M_{\text{Tot}}) \quad (9)$$

M_{Tot} could in principle vary across the surface, but for directly adsorbed fluorophores, it is entirely dominated by nonradiative decay into the metal as shown in ref 21 and is therefore approximately the same for all molecules (see also section S.III of the Supporting Information). α_B is therefore constant and only depends on the fluorophore/metal combination. For example, for Nile Blue on Gold, we can measure $Q^0 M_{\text{Tot}} = 4000$, and we can infer from $\gamma_B^0 = 3.2 \times 10^{-4} \text{ s}^{-1} \text{ W}^{-1} \text{ cm}^2$ that $\alpha_B = 8 \times 10^{-8} \text{ s}^{-1} \text{ W}^{-1} \text{ cm}^2$. If all the molecules were experiencing the same enhancement factor M , eqs 7–8 would result again in a monoexponential decay with a modified rate $\alpha_B M S_L$. Measuring experimentally this rate would in principle result in an estimate of the enhancement factor M .

Effect of the Enhancement Factor Distribution. In practice, most SERS/SEF substrates exhibit large variations of the enhancement factor on their surface, resulting in an extreme, long-tail, probability distribution $p(M)$ of enhancement factors.^{12,15,31} For example, a truncated Pareto distribution was proposed in ref 15 as a possible model. M can typically vary over at least 4 orders of magnitude, and the photobleaching rates of different molecules on the surface could therefore differ by that much. The time dependence of the SERS (or SEF) signal needs to account for this diversity through integration of the probability distribution, explicitly

$$\frac{I_{\text{SERS}}(t, S_L)}{\mu_m \sigma_{\text{Raman}}^0 P_L} = \int_{M_{\text{min}}}^{M_{\text{max}}} p(M) M^2 \exp(-\alpha_B M S_L t) dM \quad (10)$$

From this, we see that the decay of the SERS signal is somehow related to the EF distribution through an integral

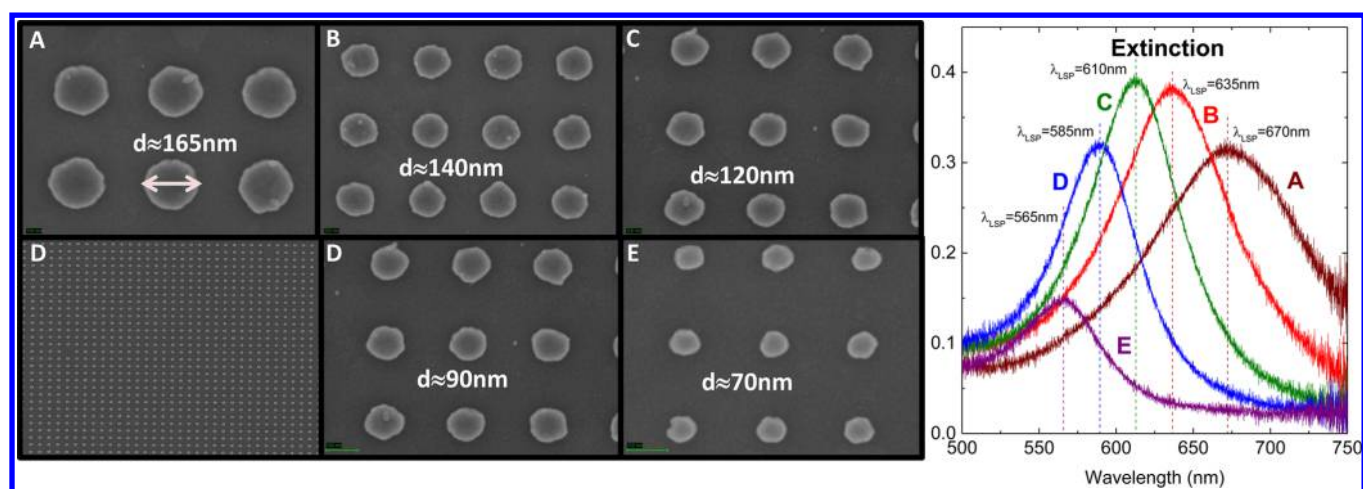


Figure 2. Gold nanodisc arrays. SEM images of the five gold nanodisc arrays used in this work and denoted A–E (a wide area image is also shown for D). The nanodisc height is 50 nm, and the diameter d is varied as indicated to tune the localized surface plasmon resonances, as evident in the extinction spectra shown on the right-hand side.

transform akin to a Laplace transform (this link is further discussed in section S.IV of the Supporting Information). The most important feature of those PB decays is that they are strongly nonexponential because of the large distribution of enhancements (and hence of photobleaching decay rates) and are therefore better analyzed on a log–log scale. Figure 1b shows two examples of such decay for two truncated Pareto distributions with a different maximum EF M_{\max} .

Nonuniform Excitation Density. An additional source of nonunique photobleaching decay rates is the possible nonuniformity of the exciting beam power density,⁴⁴ which is experimentally very common unless special care is taken. As discussed in section S.II of the Supporting Information, this can be simply included in the theoretical model presented so far. As illustrated in Figure 1b, the resulting time dependence is dramatically different. This can be simply understood since the nonuniform excitation broadens or blurs the original EF distribution. It is clear from those examples that the Gaussian beam illumination has a major impact on the experimental results (this is shown explicitly in Figure S2 of the Supporting Information) and should be taken into account in any analysis of the data. It will in fact to some extent wash-out the effect of the EF distribution, and to avoid this issue, the best solution is to carry out experiments with a uniform excitation density, which we did for this study.

■ EXPERIMENTAL VALIDATION OF THE MODEL

To study these effects experimentally, highly uniform SERS substrates are necessary. Nanolithographically prepared gold nanodisc arrays are therefore chosen as an ideal system with well-defined and tunable plasmon resonances.^{45–47} Five arrays are selected, with resonance wavelengths ranging from 670 nm down to 565 nm, ensuring a variety of enhancement conditions when excited at 633 nm. The common SERS analyte Nile Blue (NB) is then adsorbed uniformly on the gold nanodiscs for time-dependent SERRS/SEF measurements. Scanning electron microscopy (SEM) images of the nanodisc arrays and extinction spectra are shown in Figure 2. The other important experimental consideration is the uniformity of the excitation. Gaussian beam excitation is used in most standard spectroscopic setups, and as discussed earlier and in section S.II of the Supporting Information, this is clearly not desirable in the

context of PB studies. All SERRS measurements are therefore carried out with a uniform excitation within the collected area as described in the Methods section. Representative SERRS spectra of NB are shown in Figure S1 of the Supporting Information. The relative intensity of the two main Raman peaks (at 595 and 1647 cm^{-1}) is observed to remain constant as a function of both time and power densities in all experiments for a given array of nanodiscs. This suggests that there is no change in the underlying plasmon resonance.⁴⁷ Therefore, all the results presented will refer to the 595 cm^{-1} peak intensities only.

Time and Power Scaling. Because of the extreme distribution of local field enhancement factors, the variation in PB decay rates will be similarly large, possibly spanning as much as 4–5 orders of magnitude. To study this experimentally, one therefore needs to access a wide range of time scales, from very short (i.e., ~ 10 – 100 ms for the fast PB rates of molecules with high EF) to much longer (i.e., $\sim 10^5$ s for low EF molecules), which is challenging. To alleviate this issue, one can instead use the dependence of PB rates on laser power to probe the different enhancement factor regimes. For the most highly enhanced molecules, a small incident power is the most effective as the fastest PB decay rates then shift to a longer time scale regime, which can be measured using a typical CCD detector. Conversely, a high incident power is required to access the lowest enhanced molecules, which have long PB lifetimes and a low SERRS intensity. By increasing the power, we can increase the intensity and can shift the decay rates to more suitable second- or minute-long time scales. However, it is no longer suitable for the high-enhancement molecules, which then photobleach faster than the time resolution of the measurement.

In all the models presented so far, decreasing the laser power by a given factor slows down the dynamics by the same factor. Explicitly, we can write this more generally as

$$I(t, \kappa S_L) = \kappa I(\kappa t, S_L) \quad (11)$$

which is valid for any distribution of enhancement factors (and even for a nonuniform excitation). This expression can therefore be used to scale the experimental data obtained at different power densities S_L .

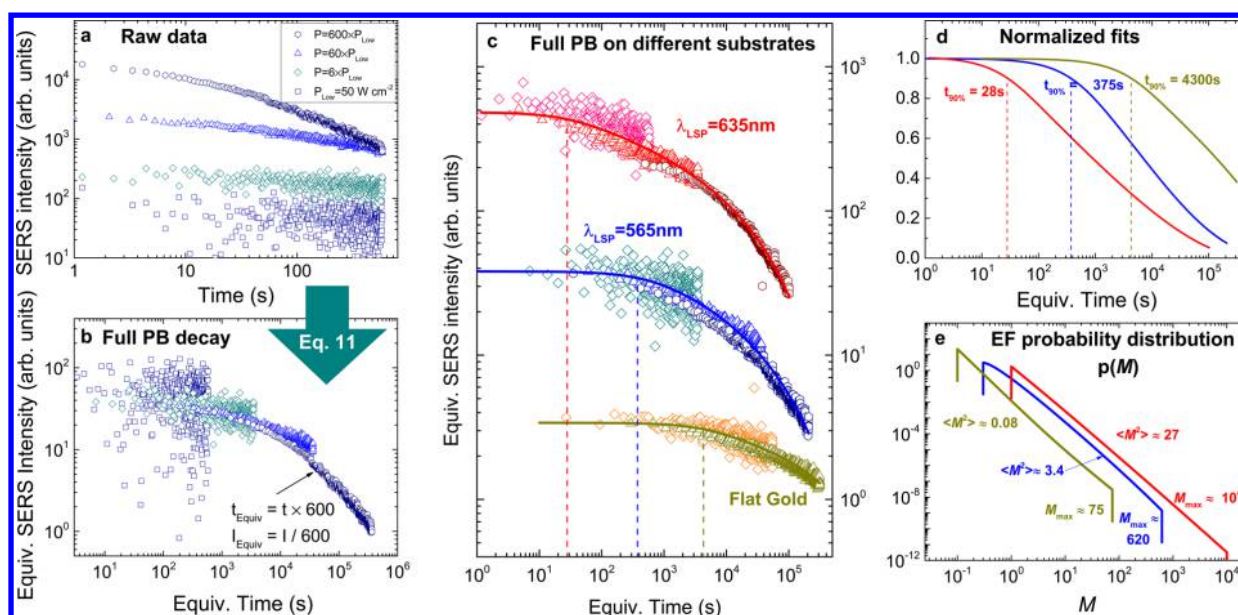


Figure 3. Experimental data and analysis. (a) Time evolution of the SERS intensity of the 595 cm^{-1} peak of NB on array E (see Figure 2) for incident powers of 50 W cm^{-2} , 300 W cm^{-2} , 3 kW cm^{-2} , and 30 kW cm^{-2} . (b) The data is then scaled in both time and intensity according to eq 11, such that they all correspond to an equivalent incident excitation of 50 W cm^{-2} . (c) Comparison of the scaled photobleaching decay for three different substrates: a flat 50 nm gold film and the nanodisc arrays E (off-resonance) and B (on-resonance, see Figure 2). Different power densities are used and scaled accordingly to obtain the dynamics over the full range of time as explained in a and b. The solid lines are a fit to the data using eq 10 as explained in section S.IV of the Supporting Information, and the probability distributions deduced from these fits are shown in e. These fits are also shown on a linear scale in d to emphasize the difference in the time of the onset of photobleaching, which is characterized for example by $t_{90\%}$, the time at which the intensity has dropped by 10%, shown as dashed lines in c and d.

To implement this approach, we carried out measurements at power densities between 30 kW cm^{-2} and 50 W cm^{-2} . In many instances, the initial decay at the highest power density is too fast to be measured by our experimental setup, but we instead measure the decay at a lower power density and scale the times and intensities according to eq 11. By scaling the data for all powers such that they are equivalent to the lowest excitation power of 50 W cm^{-2} , we can reconstruct the entire PB decay profile over many orders of magnitude in time and intensity. For example, for the largest power of 30 kW cm^{-2} , the scaling factor is 600; the dynamics should be 600 times faster and the intensities 600 times larger than at the lowest power. To deduce the equivalent decay at 50 W cm^{-2} , we therefore scale the times to $t_{\text{Equiv}} = t \times 600$ and the intensities to $I_{\text{Equiv}} = I / 600$. This approach is illustrated in Figure 3a and b, which shows a set of time-dependent SERS intensities of the 595 cm^{-1} mode of NB after being adsorbed onto array E from Figure 2. The scaling procedure results in the photobleaching decay that would be observed at 50 W cm^{-2} , under the assumption that eq 11 is valid. A direct measurement at 50 W cm^{-2} would not be possible in practice because of the long times involved (up to 10^6 s in some cases). The fact that this scaling procedure produces consistent results in overlapping regions from one power to the next is a strong indication that the models developed so far do apply to this system. However, one may also notice slight discrepancies between the two largest powers, and we will come back later to this anomalous PB regime.

Extracting the Enhancement Factor Distribution. The measured PB decay curve in Figure 3b spans more than 5 orders of magnitude in time, indicating a similar spread of lifetime and therefore of enhancement factor M . In principle, information about the enhancement factor distribution can be extracted from this PB profile. Qualitatively, the theory predicts

that the molecules with the highest EF photobleach faster, and the onset of PB should therefore occur earlier in substrates with higher maximum EF. This should be evident in the decay curves in the transition from the plateau-like region at short times to the initial decay, which is linked to the minimum PB decay rate and therefore to the maximum EF. At longer times, the PB curve is related to the EF probability distribution through the integral equation in eq 10, which is further discussed in section S.IV of the Supporting Information.

To highlight these connections, we compare in Figure 3c the PB decay measured on three substrates with different maximum EF and EF distributions, namely and in order of increasing expected EF: a flat gold film, the (off-resonance) nanodisc array E, and the (on-resonance) array B. It is clear that the onset of photobleaching occurs at a later time for lower EF substrates. One way to characterize quantitatively this onset is to consider the time $t_{90\%}$ at which the SERS signal has dropped by 10%, as shown in Figure 3d. $t_{90\%}$ should depend on the details of the EF distribution around the maximum EF, but in a rough approximation, one could expect $\alpha_B t_{90\%} M_{\text{max}} S_L \sim 1$, which suggests a scaling by a factor of about 10 each time in the M_{max} going from flat gold to nonresonant nanodiscs and then on to resonant ones.

To be more quantitative about M_{max} and the entire EF distribution, one needs to fit the PB decays using eq 10. The technical details of this fitting procedure are discussed in section S.IV of the Supporting Information. The fits we obtained are shown as solid lines in Figure 3c and d, and the EF distribution extracted from the fits are shown in Figure 3e. As expected, the maximum EFs follow the qualitative behavior discussed earlier: $\alpha_B t_{90\%} M_{\text{max}} S_L \sim 1$. Although there is much uncertainty in the derived average SERS EFs $\langle M^2 \rangle$, the value computed from these distributions should in principle be

correlated with the initial SERRS intensities (I_0 at $t = 0$). To be more precise, one has to take into account the expected number of molecules contributing to the SERRS signal. Although the absolute number is difficult to estimate, the relative coverages on each substrate can be simply computed from the known geometry of the nanodisc arrays (diameter, height, and lattice spacing). Setting a coverage $\mu = 1$ on the flat gold film, we for example have $\mu = 0.3$ for array E and $\mu = 0.48$ for array B. The relative SERRS EF at $t = 0$ would then scale as I_0/μ , that is, taking a value of 1 for flat gold, we get 38 for array E and 280 for array B. These experimental values correlate well with the ones obtained from the fits: $\langle M^2 \rangle = 0.08, 3.4,$ and 27 , respectively, lending further support to this analysis.

Discussion. A few important additional comments are worth noting:

- (1) For a given decay curve, there remains some uncertainty in the extracted maximum, minimum, and average EF, and there is even more uncertainty on the details of the distribution. This is a fundamental limitation of inverse Laplace transform problems, and such uncertainties are further increased when dealing with noisy experimental data.
- (2) The absolute values of the EFs derived from the PB decay analysis strongly depend on the assumptions made on the non-SERS photobleaching properties of the probe (which determine α_B), which are difficult to determine reliably and could anyway be modified upon adsorption on the metal surface. Conclusions regarding relative EF (between two substrates) are therefore much more reliable than those relating to absolute EFs. Nevertheless, the independent measurement of the absolute average EF at low powers can provide a means of calibration or validation of the value of α_B . We can in fact estimate experimentally the absolute SERRS EF on the flat gold substrate (see Methods) to be $\langle M^2 \rangle = 0.062$. Given the uncertainties in Nile Blue molecular coverage and inverse Laplace problems, this is in good agreement with the value of 0.08 inferred from PB decays. This provides independent justification that the value chosen for α_B is correct for Nile Blue on gold surfaces.
- (3) The average SERRS EFs (either directly measured or inferred from the PB decays) may appear quite low, which can be attributed to two concomitant effects. First, the nanodisc arrays have relatively low SERS EFs by SERS standards, with predicted average SERS EFs of $\langle M^2 \rangle \sim 5 \times 10^3$ at resonance for array B (see EM calculations in section S.V of the Supporting Information). We here choose them for their uniformity, which makes the interpretations easier, but it is a trade-off with SERS EF magnitude. In addition, like many organic dyes, Nile Blue adsorbs flat on the gold surface,⁴⁸ which dramatically reduces the local field enhancements. The predicted average SERS EFs is for example reduced to $\langle M_{\parallel}^2 \rangle \sim 27$ only for an orientation parallel to the surface, in agreement with our measurements.
- (4) The maximum SERS EFs inferred from the PB decays appear very large compared to theoretical predictions, which for example suggest $M_{\parallel-\max} \sim 7.6$ for the nanodiscs of array B or $M_{\parallel-\max} \sim 0.3$ for flat gold films. This could be partly explained by the presence of molecules standing more upright for which the predicted maximum EF is $M_{\max} \sim 260$ for array B. The remaining

discrepancy can be attributed to the sharp edges of the nanodiscs (which are not accounted for in the model) or to the presence of special sites of larger enhancement, perhaps linked to the unavoidable roughness of the metal surface on the nanometer scale. The important point is that those special upright molecules and those on special sites are quite rare, owing to the extreme long-tail nature of the derived distributions (Figure 3e). For example, focusing on array B, the probability that M is larger than 7.6 is in fact only $p(M > 7.6) \sim 3\%$ and similarly $p(M > 260) \sim 2.5 \times 10^{-5}$ only. Similarly on flat gold, we infer from the derived distribution that $p(M > 0.3) = 8\%$ only. We conclude that the PB decay at the lower powers is dominated by a remarkably small number of molecules at special sites or in a special configuration/orientation. The PB study allows access to information about those rare molecules, which would be very difficult with any other technique.

In summary, our experimental results and the analysis of the PB decay curves provide strong support for the theoretical model summarized in eq 10 and demonstrate the possibility of exploiting photobleaching to extract information about the EF distribution.

■ ANOMALOUS PHOTBLEACHING REGIME

Further Evidence of Anomalous Photobleaching. The scaling law (eq 11) discussed earlier as evidence for the theoretical model can equally be used to demonstrate deviations from it. This was perhaps evident from the nonperfect overlapping of the data at the highest power density in Figure 3b. To better understand the impact that high incident powers have, we investigated the scaling behavior on all the nanodisc arrays of Figure 2, each with different resonance wavelengths and therefore maximum EF. Figure 4a–e shows the scaled time-dependent SERRS intensity profiles for six incident powers and for five different arrays of structures with plasmon resonance wavelengths λ_{LSP} varying between 670 and 565 nm (see Figure 2 for the extinction spectra). When λ_{LSP} is far from the incident wavelength (633 nm), the different power curves are in close agreement (as seen earlier on array E, $\lambda_{\text{LSP}} = 565$ nm). This is not the case closer to the plasmon resonance wavelength (array B and C, $\lambda_{\text{LSP}} = 635$ and 610 nm) where we observe a significant offset in the initial intensity for the highest incident powers, followed by a much steeper decrease in the intensity profile relative to the low-power curves. Note again that because of the applied scaling (eq 11), all these curves should be superimposed. We conclude that there is an anomalous photobleaching regime, which is more evident from the more enhancing samples, that is, it is not only dependent on laser power but also on the resonance properties of the substrate.

To explain these modifications to the expected PB decay profile at high incident powers, we can consider two broad classes of mechanisms for which the predicted effects on the PB decay curves are shown in Figure 4f:

- (1) Local effects. Given that the effect is most prominent for high powers and more resonant structures, it is natural to consider first mechanisms that would more strongly affect the molecules experiencing the highest EF. Second-order optical effects would fit in this category, and it is, for example, believed that two-photon absorption may play a role in dye PB at higher power densities.⁴⁹ This

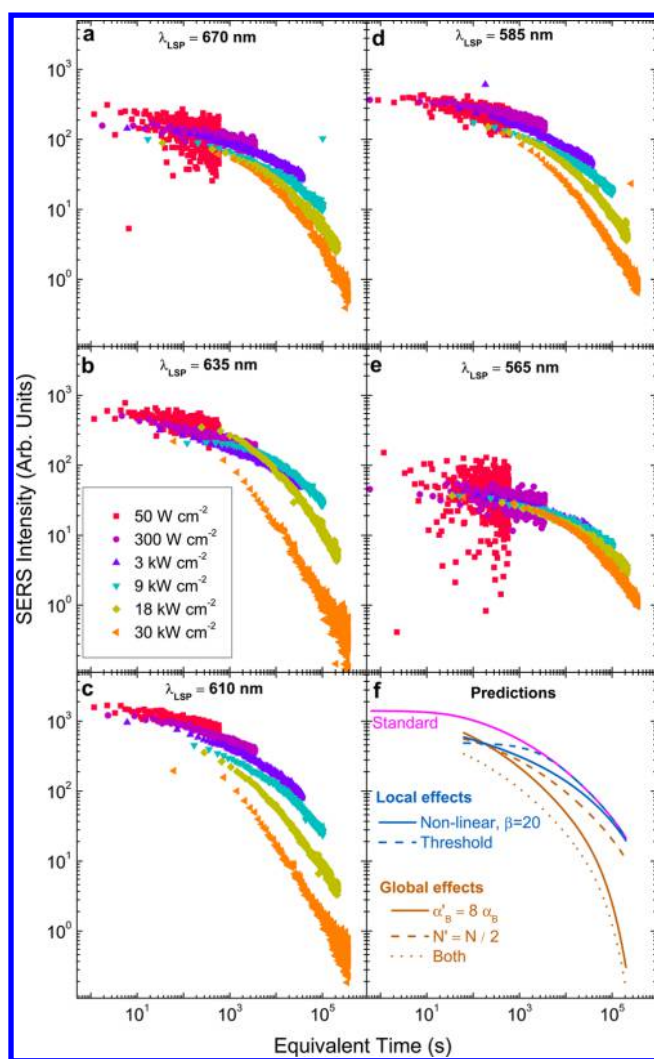


Figure 4. Anomalous photobleaching regime. (a–e) Photobleaching decay curves obtained by scaling the SERRS intensities and times for six different excitation power densities for each of the five nanodisc arrays shown in Figure 2. Equivalent time corresponds to what would be observed at the lowest power density of 50 W cm^{-2} according to eq 11. (f) Theoretical prediction of the PB decay curves in the standard model of PB discussed so far and compared with proposed modifications including: (1) two-photon optical processes, which would modify the PB rate from $\alpha_B MS_L$ to $\alpha_B MS_L + \beta(\alpha_B MS_L)^2$, with $\beta = 20$ here; (2) a threshold in which all molecules for which $MS_L > I_{\text{Thr}} = 4 \times 10^6 \text{ W cm}^{-2}$ are destroyed (or desorbed); (3) a global change in the intrinsic PB rate to $\alpha'_B = 8\alpha_B$; (4) a global change in the absorption cross section or in the number of molecules to $N' = N/2$, resulting in a simple scaling of the SERRS intensity $I'(t) = I(t)/2$; (5) the latter two together. The enhancement factor distribution used for f is the one obtained from a fit of the PB decay curve observed at low power densities on array C ($\lambda_{\text{LSP}} = 610 \text{ nm}$).

mechanism would result in an increase in the PB rate because of an additional nonlinear term, that is, $\exp[-(\alpha_B MS_L + \beta \alpha_B^2 M^2 S_L^2)t]$ instead of $\exp(-\alpha_B MS_L t)$ in eq 10. Alternatively, one could also consider a threshold field intensity I_{Thr} above which the fluorophores are immediately destroyed, that is, when $MI_L > I_{\text{Thr}}$. Such a mechanism was, for example, invoked in ref 12 for nonresonant molecules. All these local effect scenarios would selectively target those molecules with

the highest EF and would also be more prominent for the higher power densities.

- (2) Global effects. In addition, we can consider alternative mechanisms affecting equally all the molecules that are adsorbed onto the gold surface and not only the ones with the highest EF. The most obvious example is a change in temperature of the nanostructures as a result of laser heating via optical absorption in the metal.^{50–52} This would be more pronounced for the more resonant nanostructures, as observed. Exactly how this temperature increase will impact the PB dynamics of our system may be complex, but it could, for example, involve a change in the quantum yield⁵³ as well as in the reactivity of the dye with the surrounding environment.⁵⁴ The overall effect will be a modification of α_B and should manifest experimentally as a change in the PB dynamics of all the molecules (i.e., at all delay times and not only in the initial stages). An alternative global effect that may be considered is that of thermally induced desorption, which would result for the largest powers in a decrease in the number of adsorbed molecules. This would again affect all the molecules.

As suggested by the predictions of Figure 4f, the possible mechanisms for anomalous PB can be distinguished experimentally. For local effects, one would qualitatively expect that after a long time of high power irradiation, the intensity profile will converge toward the intensity profile of the lower irradiation power as only the less enhanced molecules have survived. For global effects, however, the curves should remain well separated. The results in Figure 1a–e clearly prove that the latter occurs, which strongly suggests that the anomalous PB regime corresponds to a global modification of the PB dynamics.

Heating Effects. The most likely explanation for the latter is laser-induced heating effects,^{50–52} which we investigated further by measuring the ratio of anti-Stokes and Stokes SERRS intensities, ρ , as anti-Stokes scattering is dependent on the thermal vibrational population. Figure 5a demonstrates that for the six powers used in these experiments, ρ is approximately constant with time. This is not surprising as any temperature increase should stabilize very rapidly (faster than $\sim \mu\text{s}$ given the thermal diffusivity of gold). Furthermore, ρ and, therefore, the fluorophore and nanodisc temperature T_f increase significantly for the highest excitation powers and, in fact, precisely for those where anomalous PB is observed. We can in fact deduce T_f from the anti-Stokes/Stokes ratio (see section S.VI of the Supporting Information), and these are shown as a function of incident power in Figure 5b for the five nanodisc arrays. There is a substantial increase in T_f when exciting close to the plasmon resonance. The largest calculated temperature is $\sim 480 \text{ K}$ which is an increase of $\sim 200 \text{ K}$ above room temperature. At these temperatures, we can expect that there will be a significant modification of the PB dynamics because of changes in the quantum yield and chemical reactivity. A comparison with Figure 4 suggests that the deviation of the intensity profile from the expected curve is directly correlated to the measured temperature increase, with the largest deviation occurring for array B and C, which further confirms that the anomalous PB regime is linked to the temperature increase. The largest increase is obtained for array C ($\lambda_{\text{LSP}} = 610 \text{ nm}$) rather than for the more resonant array B ($\lambda_{\text{LSP}} = 635 \text{ nm}$). We attribute this to the different volume of the nanodiscs, which is larger for

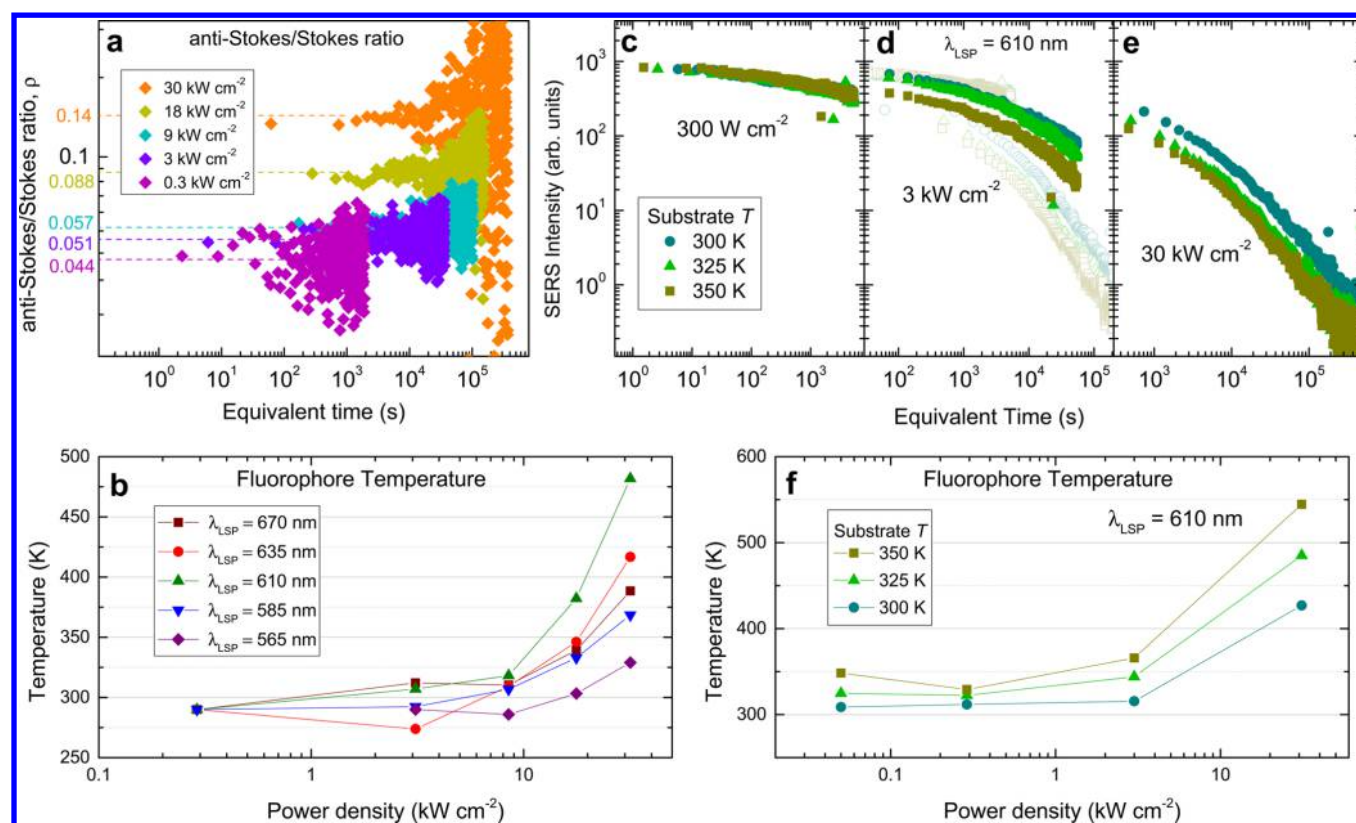


Figure 5. Temperature measurements. (a) Anti-Stokes to Stokes intensity ratio as a function of time for the 610 nm resonant nanodiscs and different incident power densities. (b) Nile Blue temperature T_f estimated from the average of the anti-Stokes to Stokes ratio (corrected by the asymmetry factor, see section S.VI of the Supporting Information) of the first 50 points for each of the five sets of structures. (c–e) SERRS intensity decay curves for substrate temperatures of 300, 325, and 350 K and incident powers of (c) 300 W cm^{-2} , (d) 3 kW cm^{-2} , and (e) 30 kW cm^{-2} . In d are also reproduced in a lighter shade the data of c and e to facilitate their comparison. (f) Power dependence of the molecular temperature T_f as estimated from the anti-Stokes to Stokes intensity ratio for the three substrate temperatures.

B, meaning that it requires more energy to heat and that the absorption-to-scattering ratio is also smaller.

To further understand the heating effect, we focused on array C and carried out experiments where the sample temperature was increased externally using a hot plate, while keeping the illumination intensity constant. Figure 5c–e shows the PB decays for varying powers and substrate temperatures. The temperature of the fluorophores, as calculated from the anti-Stokes to Stokes intensity ratio, is also shown in Figure 5f. For the lowest incident power of 300 W cm^{-2} , the measured temperature of the molecules is the same within experimental uncertainties as the substrate temperature. The PB decay profile is approximately the same for substrate temperatures of 300, 325, and 350 K (see Figure 5c), which suggests that temperature does not have a noticeable impact on the PB dynamics up to 350 K. For a power density of 3 kW cm^{-2} , we start to observe laser-induced heating with small NB temperature increases of $\sim 15 \text{ K}$. While the intensity profiles at 300 and 325 K are similar, there is a substantial decrease in overall intensity for NB temperatures of 365 K (350 K hot plate). This suggests that there is a change in the intensity profile over a relatively small shift in temperature and given that the curves are parallel, it may be associated with a loss of population, for example, because of desorption. Finally, for the largest power density of 30 kW cm^{-2} , the measured NB temperature variation is much larger (between 430 and 550 K). Yet, the intensity profiles only show a small decrease from one curve to the next (Figure 5e). In all three cases, however, the decays appear faster

than one would have expected by extrapolating the lower power curves, which suggests a change in the PB properties (in this case, multiplying α_B by a factor of 8 can account for the change, see Figure 4f).

These results suggest that laser-induced heating affects the PB decay profiles in at least two ways. For large temperature increases ($>400 \text{ K}$), there is an increase in the intrinsic PB decay rate characterized by α_B . At lower temperatures, there appears to be a sudden loss of intensity over a relatively small temperature range just above 350 K. This could be due to thermally induced reorientation or desorption of a subset of the adsorbed molecules. Given the temperature where this occurs, we may speculate that it occurs at 373 K, the boiling point of water, and would then be related to changes in the properties of NB induced by the presence/absence of nearby water molecules.

DISCUSSION AND CONCLUSION

In this paper, we have extensively investigated the photobleaching dynamics of fluorophores on metallic nanostructures supporting plasmon resonances. We specifically focused on the system of Nile Blue adsorbed on uniform arrays of gold nanodiscs, using the SERRS signal as a reporter of Nile Blue population, but the conclusions are expected to be much more general. We showed that PB decays are strongly sensitive to both incident power density and the resonance wavelength of the structures. At low and medium incident powers, the results can be understood within a standard photobleaching

mechanism mediated by intersystem crossing, providing that all the plasmon-induced modifications to the EM transitions rates are duly taken into account. A direct consequence of this model is that the extreme nature of the enhancement factor distribution on the surface results in a wide range of PB decay rates (over several orders of magnitude). This was clearly evidenced in the nonexponential nature of the decays, and we introduced a method based on scaling of time and intensities at different powers to measure these decays over more than 5 orders of magnitude in time. We discussed how those decays can be exploited to measure the EF distribution and in particular the maximum EF, which are typically very difficult to access experimentally. This analysis revealed that the maximum EF and the associated initial PB decay rates strongly depend on a remarkably small number of molecules with particularly large EF, perhaps because of their orientation or their location at rare sites on the surface.

Finally, we also observed an anomalous photobleaching regime at higher powers, which upon further scrutiny could be attributed to heating of the nanodiscs through plasmon-enhanced absorption in gold at resonance. This problem may not be present in all systems and indeed could be dramatically reduced by working in aqueous solutions, where heat dissipation would be much more efficient. Nevertheless, it clearly highlights the difficulty in decoupling standard photobleaching mechanisms from potential additional effects occurring at larger powers in resonant plasmonic nanostructures.

Given the common occurrence of photobleaching problems, the results of this work will be important to most studies and practical application of SERS/SEF with fluorophores. Its impact will be particularly important in several contexts, including: (1) Mitigating PB effects: photodegradation in general is a major impediment in most applications of SERS/SEF and the most common way around it is to reduce the excitation power to avoid it, or at least limit it. But this in turn reduces the sensitivity and limit of detection, which are critical in many experiments and for single-molecule detection in particular. Understanding the mechanisms of PB on metallic surfaces is the first step toward developing new routes to alleviate, if not eliminate, these issues. (2) The study of alternative mechanisms of PB (for example for nonresonant molecules) and how they relate to the EF distribution. (3) Looking further afield, the understanding of the link between EF distributions and PB will also benefit recent efforts to exploit surface-enhancements and EM hot-spots for other types of photochemical reactions.^{5,16,17}

METHODS

Sample Preparation. The samples were fabricated by standard positive-resist (950k PMMA) electron beam lithography on a Zeiss SUPRA 40 field emission scanning electron microscope operated at 30 kV. The development of the exposed resist was done by dipping the substrate in a 1:3 methyl isobutyl ketone/isopropanol solution for 30 s. A 50 nm layer of gold was then thermally evaporated onto the substrate, followed by lift-off in acetone. No adhesion layer was used between the ITO substrate and the gold particles. Gold nanodiscs of diameters varying between 70 nm (array E) and 150 nm (array A) were fabricated. Each set of nanodiscs was arrayed over a $80\ \mu\text{m} \times 80\ \mu\text{m}$ region in a square lattice with spacings of (from array A to array E) 300, 280, 260, 240, and 220 nm, respectively. This resulted in varying plasmon resonance wavelengths ranging from 670 to 565 nm (after

Nile Blue deposition) ensuring that we had a variety of enhancement conditions when illuminating with a 633 nm helium–neon laser.^{45–47} SEM images of the structures are shown in Figure 2. The flat gold film substrates (50 nm thick on a glass slide) were purchased from Ssens. Nile Blue (NB) was adsorbed onto the metallic surfaces by placing a $20\ \mu\text{L}$ droplet of $10\ \mu\text{M}$ NB solution in water on the substrate for a period of 10 min before rinsing with water. The droplet was centered over the structures to ensure a homogeneous deposition of dyes over the arrayed structures.

SERRS Measurements. After sample preparation, the substrate was placed on the translation stage of a LabRam Raman spectrometer with a 600 L/mm grating and a liquid-N₂-cooled CCD. A 633 nm HeNe laser was used for excitation, with a maximum power of 4.5 mW at the sample. Filters were used to reduce the power as desired. All Raman measurements were carried out in air in the backscattering configuration with the nanodisc arrays in the focal plane of a $\times 100$ 0.9 NA air objective. To ensure uniform excitation, two steps were taken: (1) A 400 mm focal lens was placed before the notch filter to focus the incident beam onto the back focal plane of the microscope objective, resulting in a larger spot size on the sample (with a Gaussian profile of waist $w_0 \sim 3\ \mu\text{m}$); (2) The (square-shaped) confocal pinhole was reduced in size until there was a factor of ~ 10 drop in overall intensity. This procedure ensured that we were only collecting from the uniform region in the center of the Gaussian beam (see schematic in Figure 1b). From the drop (by a factor of ~ 10) in collected intensity, we inferred that the power density at the edge of the collected area was still 83% of that in the center. For anti-Stokes to Stokes ratio measurements, the spectrometer was centered at 633 nm so that the $595\ \text{cm}^{-1}$ anti-Stokes and Stokes peaks could be observed simultaneously.

Extinction Spectra. Extinction spectra were measured after Nile Blue deposition using the LabRam spectrometer and a halogen lamp in transmission configuration (illuminating from underneath the sample). The $\times 100$ 0.9NA air objective was used to collect the transmitted light which was redirected, without the use of a notch filter, to the monochromator. A reference spectrum was taken on the ITO surface surrounding the Au nanodiscs. A multiwindow scan was performed in order to encompass the full spectral range of the localized surface plasmon resonance.

Average SERS EF. Nitrogen gas in air was used as a reference Raman standard (with differential Raman cross section of $1.6 \times 10^{-31}\ \text{cm}^2/\text{sr}$ at 633 nm¹). The scattering volume was characterized as in ref 41, and the Nile Blue surface coverage was taken as^{48,55} $\mu_{\text{m}} = 5.5 \times 10^{-11}\ \text{mol}/\text{cm}^2$. To obtain the average SERS EF, the average SERRS cross section was then normalized to the Nile Blue cross section of the $595\ \text{cm}^{-1}$ mode at 633 nm in air of $6.8 \times 10^{-25}\ \text{cm}^2/\text{sr}$, estimated from the measured cross section in water⁵⁶ corrected by the local field-correction factor for water of 2.5.¹

ASSOCIATED CONTENT

Supporting Information

Additional details on the fluorescence and SERRS properties of Nile Blue, the effect of a Gaussian beam excitation, the experimental determination of M_{Tot} , the numerical procedure for the inverse Laplace transform, electromagnetic calculations of enhancements, and temperature determination from anti-Stokes measurements. This material is available free of charge via the Internet at <http://pubs.acs.org/>.

■ AUTHOR INFORMATION

Corresponding Author

*E-mail: Eric.LeRu@vuw.ac.nz.

Notes

The authors declare no competing financial interest.

■ ACKNOWLEDGMENTS

E.C.L.R. is indebted to the Royal Society of New Zealand (RSNZ) for support through a Marsden Grant and Rutherford Discovery Fellowship.

■ REFERENCES

- (1) Le Ru, E. C.; Etchegoin, P. G. *Principles of surface-enhanced Raman spectroscopy and related plasmonic effects*; Elsevier: Amsterdam, 2009.
- (2) Watanabe, K.; Menzel, D.; Nilius, N.; Freund, H.-J. Photochemistry on metal nanoparticles. *Chem. Rev.* **2006**, *106*, 4301–4320.
- (3) Linic, S.; Ingram, P. C. D. B. Plasmonic-metal nanostructures for efficient conversion of solar to chemical energy. *Nat. Mater.* **2011**, *10*, 911–921.
- (4) Ueno, K.; Misawa, H. Surface plasmon-enhanced photochemical reactions. *J. Photochem. Photobiol., C: Photochem. Rev.* **2013**, *15*, 31–52.
- (5) Kleinman, S. L.; Frontiera, R. R.; Henry, A.-I.; Dieringer, J. A.; Van Duyne, R. P. Creating, characterizing, and controlling chemistry with SERS hot spots. *Phys. Chem. Chem. Phys.* **2013**, *15*, 21–36.
- (6) Lippincott-Schwartz, J.; Altan-Bonnet, N.; Patterson, G. H. Review: Photobleaching and photoactivation: Following protein dynamics in living cells. *Nat. Cell Biol.* **2003**, *5*, S7–S14.
- (7) Merlen, A.; Lagugne-Labarthe, F.; Harté, E. Surface-enhanced Raman and fluorescence spectroscopy of dye molecules deposited on nanostructured gold surfaces. *J. Phys. Chem. C* **2010**, *114*, 12878.
- (8) Wolkow, R. A.; Moskovits, M. Enhanced photochemistry on silver surfaces. *J. Chem. Phys.* **1987**, *87*.
- (9) Bjerneld, E. J.; Svedberg, F.; Johansson, P.; Käll, M. Direct observation of heterogeneous photochemistry on aggregated Ag nanocrystals using Raman spectroscopy: The case of photoinduced degradation of aromatic amino acids. *J. Phys. Chem. A* **2004**, *108*, 4187–4193.
- (10) Le Ru, E. C.; Etchegoin, P. G. Sub-wavelength localization of hot-spots in SERS. *Chem. Phys. Lett.* **2004**, *396*, 393–397.
- (11) Etchegoin, P. G.; Lacharmoise, P. D.; Le Ru, E. C. Influence of photostability on single-molecule surface enhanced Raman scattering enhancement factors. *Anal. Chem.* **2009**, *81*, 682–688.
- (12) Fang, Y.; Seong, N.-H.; Dlott, D. D. Measurement of the distribution of site enhancements in surface-enhanced Raman scattering. *Science* **2008**, *321*, 388–392.
- (13) Nitzan, A.; Brus, L. E. Theoretical model for enhanced photochemistry on rough surfaces. *J. Chem. Phys.* **1981**, *75*, 2205–2214.
- (14) Vasilev, K.; Stefani, F. D.; Jacobsen, V.; Knoll, W.; Kreiter, M. Reduced photobleaching of chromophores close to a metal surface. *J. Chem. Phys.* **2004**, *120*, 6701–6704.
- (15) Le Ru, E. C.; Etchegoin, P. G.; Meyer, M. Enhancement factor distribution around a single surface-enhanced Raman scattering hot spot and its relation to single molecule detection. *J. Chem. Phys.* **2006**, *125*, 204701.
- (16) Hubert, C.; Rumyantseva, A.; Lerondel, G.; Grand, J.; Kostcheev, S.; Billot, L.; Vial, A.; Bachelot, R.; Royer, P.; Chang, S.-H.; et al. Near-field photochemical imaging of noble metal nanostructures. *Nano Lett.* **2005**, *5*, 615–619.
- (17) Xu, S.; Shan, J.; Shi, W.; Liu, L.; Xu, L. Modifying photoisomerization efficiency by metallic nanostructures. *Opt. Express* **2011**, *19*, 12336–12341.
- (18) Das, P.; Metiu, H. Enhancement of molecular fluorescence and photochemistry by small metal particles. *J. Phys. Chem.* **1985**, *89*, 4680–4687.
- (19) Pettinger, B.; Ren, B.; Picardi, G.; Schuster, R.; Ertl, G. Tip-enhanced Raman spectroscopy (TERS) of malachite green isothiocyanate at Au(111): Bleaching behavior under the influence of high electromagnetic fields. *J. Raman Spectrosc.* **2005**, *36*, 541–550.
- (20) Maher, R. C.; Zhang, T.; Cohen, L. F.; Gallop, J. C.; Liu, F. M.; Green, M. Towards a metrological determination of the performance of SERS media. *Phys. Chem. Chem. Phys.* **2009**, *11*, 7463–7468.
- (21) Galloway, C. M.; Etchegoin, P. G.; Le Ru, E. C. Ultrafast nonradiative decay rates on metallic surfaces by comparing surface-enhanced Raman and fluorescence signals of single molecules. *Phys. Rev. Lett.* **2009**, *103*, 063003.
- (22) Moskovits, M. Surface-enhanced spectroscopy. *Rev. Mod. Phys.* **1985**, *57*, 783–825.
- (23) Le Ru, E. C.; Etchegoin, P. G. Rigorous justification of the $|E|^4$ enhancement factor in surface enhanced Raman spectroscopy. *Chem. Phys. Lett.* **2006**, *423*, 63–66.
- (24) Le Ru, E. C.; Etchegoin, P. G.; Grand, J.; Félidj, N.; Aubard, J.; Lévi, G. Mechanisms of spectral profile modification in surface-enhanced fluorescence. *J. Phys. Chem. C* **2007**, *111*, 16076–16079.
- (25) Bharadwaj, P.; Novotny, L. Spectral dependence of single molecule fluorescence enhancement. *Opt. Express* **2007**, *15*, 14266–14274.
- (26) Gill, R.; Le Ru, E. C. Fluorescence enhancement at hot-spots: The case of Ag nanoparticle aggregates. *Phys. Chem. Chem. Phys.* **2011**, *13*, 16366–16372.
- (27) Le Ru, E. C.; Grand, J.; Félidj, N.; Aubard, J.; Lévi, G.; Hohenau, A.; Krenn, J. R.; Blackie, E.; Etchegoin, P. G. Spectral profile modifications in metal-enhanced fluorescence. *Met.-Enhanced Fluoresc.* **2010**, 25–65.
- (28) Carminati, R.; Greffet, J.-J.; Henkel, C.; Vigoureux, J. Radiative and non-radiative decay of a single molecule close to a metallic nanoparticle. *Opt. Commun.* **2006**, *261*, 368–375.
- (29) Moroz, A. Non-radiative decay of a dipole emitter close to a metallic nanoparticle: Importance of higher-order multipole contributions. *Opt. Commun.* **2010**, *283*, 2277–2287.
- (30) Gill, R.; Tian, L.; Somerville, W. R. C.; Le Ru, E. C.; van Amerongen, H.; Subramaniam, V. Silver nanoparticle aggregates as highly efficient plasmonic antennas for fluorescence enhancement. *J. Phys. Chem. C* **2012**, *116*, 16687–16693.
- (31) Le Ru, E. C.; Etchegoin, P. G. Phenomenological local field enhancement factor distributions around electromagnetic hot spots. *J. Chem. Phys.* **2009**, *130*, 181101.
- (32) Laurence, T. A.; Braun, G. B.; Reich, N. O.; Moskovits, M. Robust SERS enhancement factor statistics using rotational correlation spectroscopy. *Nano Lett.* **2012**, *12*, 2912–2917.
- (33) Kasche, V.; Linqvist, L. Reactions between the triplet state of fluorescein and oxygen. *J. Phys. Chem.* **1964**, *68*, 817–823.
- (34) Song, L.; Hennink, E. J.; Young, I. T.; Tanke, H. J. Photobleaching kinetics of fluorescein in quantitative fluorescence microscopy. *Biophys. J.* **1995**, *68*, 2588–2600.
- (35) Soumpasis, D. M. Theoretical analysis of fluorescence photobleaching recovery experiments. *Biophys. J.* **1983**, *41*, 95–97.
- (36) Usui, Y.; Itoh, K.; Koizumi. Switch-over of the mechanism of the primary processes in the photo-oxidation of xanthene dyes as revealed by the oxygen consumption experiments. *Bull. Chem. Soc. Jpn.* **1965**, *38*, 1015–1022.
- (37) Widengren, J.; Mets, U.; Rigler, R. Fluorescence correlation spectroscopy of triplet states in solution: A theoretical and experimental study. *J. Phys. Chem.* **1995**, *99*, 13368–13379.
- (38) Widengren, J.; Rigler, R. Mechanisms of photobleaching investigated by fluorescence correlation spectroscopy. *Bioimaging* **1996**, *4*, 149–157.
- (39) Deschenes, L. A.; Vanden Bout, D. A. Single molecule photobleaching: Increasing photon yield and survival time through suppression of two-step photolysis. *Chem. Phys. Lett.* **2002**, *365*, 387–395.
- (40) Guo, L.; Gai, F. Simple method to enhance the photostability of the fluorescence reporter R6G for prolonged single-molecule studies. *J. Phys. Chem. A* **2013**, *117*, 6164–6170.

(41) Le Ru, E. C.; Blackie, E.; Meyer, M.; Etchegoin, P. G. Surface Enhanced Raman Scattering enhancement factors: A comprehensive study. *J. Phys. Chem. C* **2007**, *111*, 13794–13803.

(42) Zhang, Y.; Aslan, K.; Previte, M. J. R.; Geddes, C. D. Metal-enhanced singlet oxygen generation: A consequence of plasmon enhanced triplet yields. *J. Fluoresc.* **2007**, *17*, 345–349.

(43) Zhang, Y.; Aslan, K.; Previte, M. J. R.; Malyn, S. N.; Geddes, C. D. Metal-enhanced phosphorescence: Interpretation in terms of triplet-coupled radiating plasmons. *J. Phys. Chem. B* **2006**, *110*, 25108–25114.

(44) Berglund, A. J. Nonexponential statistics of fluorescence photobleaching. *J. Chem. Phys.* **2004**, *121*, 2899–2903.

(45) Félidj, N.; Aubard, J.; Lévi, G.; Krenn, J. R.; Hohenau, A.; Schider, G.; Leitner, A.; Aussenegg, F. R. Optimized surface-enhanced Raman scattering on gold nanoparticle arrays. *Appl. Phys. Lett.* **2003**, *82*, 3095–3097.

(46) Félidj, N.; Aubard, J.; Lévi, G.; Krenn, J. R.; Salerno, M.; Schider, G.; Lamprecht, B.; Leitner, A.; Aussenegg, F. R. Controlling the optical response of regular arrays of gold particles for surface-enhanced Raman scattering. *Phys. Rev. B* **2002**, *65*, 075419.

(47) Le Ru, E. C.; Etchegoin, P. G.; Grand, J.; Félidj, N.; Aubard, J.; Lévi, G.; Hohenau, A.; Krenn, J. R. Surface enhanced Raman spectroscopy on nanolithography-prepared substrates. *Curr. Appl. Phys.* **2008**, *8*, 467–470.

(48) Le Ru, E. C.; Meyer, S. A.; Artur, C.; Etchegoin, P. G.; Grand, J.; Lang, P.; Maurel, F. Experimental demonstration of surface selection rules for SERS on flat metallic surfaces. *Chem. Commun.* **2011**, *47*, 3903–3905.

(49) Eggeling, C.; Widengren, J.; Rigler, R.; Seidel, C. A. M. Photobleaching of fluorescent dyes under conditions used for single-molecule detection: Evidence of two-step photolysis. *Anal. Chem.* **1998**, *70*, 2651–2659.

(50) Govorov, A.; Zhang, W.; Skeini, T.; Richardson, H.; Lee, J.; Kotov, N. Gold nanoparticle ensembles as heaters and actuators: Melting and collective plasmon resonances. *Nanoscale Res. Lett.* **2006**, *1*, 84–90.

(51) Baffou, G.; Girard, C.; Quidant, R. Mapping heat origin in plasmonic structures. *Phys. Rev. Lett.* **2010**, *104*, 136805.

(52) Baffou, G.; Berto, P.; Bermúdez Ureña, E.; Quidant, R.; Monneret, S.; Polleux, J.; Rigneault, H. Photoinduced heating of nanoparticle arrays. *ACS Nano* **2013**, *7*, 6478–6488.

(53) Grofcsik, A.; Kubinyi, M.; Jones, W. J. Fluorescence decay dynamics of organic dye molecules in solution. *J. Mol. Struct.* **1995**, *348*, 197–200.

(54) Viets, C.; Hill, W. Laser power effects in SERS spectroscopy at thin metal films. *J. Phys. Chem. B* **2001**, *105*, 6330–6336.

(55) Kuramitz, H.; Sugawara, K.; Kawasaki, M.; Hasebe, K.; Nakamura, H.; Tanaka, S. Electrocatalytic reduction of Hemoglobin at a self-assembled monolayer electrode containing redox dye, Nile Blue as an electron-transfer mediator. *Anal. Sci.* **1999**, *15*, 589.

(56) Reigue, A.; Auguie, B.; Etchegoin, P. G.; Le Ru, E. C. CW measurements of resonance Raman profiles, line-widths, and cross-sections of fluorescent dyes: Application to Nile Blue A in water and ethanol. *J. Raman Spectrosc.* **2013**, *44*, 573–581.

Supporting information for “Photobleaching of fluorophores on the surface of nanoantennas”

C. M. Galloway and C. Artur

The MacDiarmid Institute for Advanced Materials and Nanotechnology, School of Chemical and Physical Sciences, Victoria University of Wellington, PO Box 600 Wellington 6140, New Zealand

J. Grand

Université Paris Diderot, Sorbonne Paris Cité, ITODYS, UMR CNRS 7086, 15 rue J-A de Baïf, 75205 Paris Cedex 13, France

E. C. Le Ru*

The MacDiarmid Institute for Advanced Materials and Nanotechnology, School of Chemical and Physical Sciences, Victoria University of Wellington, PO Box 600 Wellington 6140, New Zealand

S.I. SPECTROSCOPIC PROPERTIES OF NILE BLUE

The molecule that was chosen for this study was Nile Blue A because it has an electronic transition close to the wavelength of the laser excitation (633 nm).

A. Fluorescence and photobleaching properties

To fix ideas, we provide below approximate values for the parameters relevant to the photobleaching (PB) model for NB in water (see Fig. 1):

- The excited state lifetime is of the order $(\Gamma_{\text{Tot}}^0)^{-1} \approx 400$ ps [1], which together with a quantum yield of $Q^0 = 4\%$ [2] gives a radiative lifetime of $(\Gamma_{\text{Rad}}^0)^{-1} \approx 10$ ns.
- The absorption cross-section at 633 nm is [2] $\sigma_{\text{Abs}}^0 = 2.5 \times 10^{-16}$ cm². For an excitation density of $S_L = 30$ kW cm⁻², this corresponds to an absorption rate of $\Gamma_{\text{Abs}} = (42 \text{ ns})^{-1}$.
- Typical values for the inter-system crossing lifetime [3], $(\Gamma_{\text{ISC}})^{-1}$, and triplet relaxation lifetime, $(\Gamma_T)^{-1}$, are of the order of 1 μ s while the probability per unit time of destruction while in the triplet state Γ_{TB} correspond to a longer lifetime of the order of 10 ms. From those, one can derive the photobleaching quantum yield as [4]

$$\phi_B^0 = \frac{\Gamma_{\text{ISC}} \Gamma_{TB}}{\Gamma_{\text{Tot}}^0 \Gamma_T}, \quad (\text{S1})$$

which results in $\phi_B^0 \approx 1 - 2 \times 10^{-6}$ for a good fluorophore like Rhodamine 6G [5]. This means that one Rhodamine 6G dye will on average go through $\sim 10^6$ excitation/emission cycles before

photobleaching. No data is available for Nile Blue, but triplet transition rates for oxazine dyes are known to be as low as for xanthene dyes [3, 6], so taking into account the difference in excited lifetime (4 ns for Rhodamine 6G [5]), we would deduce that ϕ_B^0 is of the order of 2×10^{-7} . We will here assume a value of $\phi_B^0 = 4 \times 10^{-7}$, adjusted using the control photobleaching experiments on flat-gold (see main text). Note that although the PB quantum yield is lower than that of Rhodamine 6G by a factor of ~ 2.5 , about 10 times fewer photons are emitted before photobleaching because of the lower quantum yield of 4%.

- From the above values, the photobleaching decay rate at $S_L = 30$ kW cm⁻² can be expected to be of the order of $\Gamma_B^0 = \Gamma_{\text{Abs}}^0 \phi_B^0 \approx 10$ s⁻¹, i.e. a lifetime of 100 ms. More generally, we may write $\Gamma_B^0 = \gamma_B^0 S_L$ with $\gamma_B^0 = 3.2 \times 10^{-4}$ s⁻¹ W⁻¹ cm².

B. SERRS spectra

Representative SERRS spectra of NB excited at 633 nm are shown in Fig. S1. Two dominant Raman peaks are observed [2], the first at 595 cm⁻¹ corresponding to a collective ring-breathing mode of the structure and the other at 1647 cm⁻¹ attributed to a NH₂ deformation. Peak intensities are estimated by integrating over the peak width whilst the Raman to fluorescence ratio is measured from the ratio of the SERRS and SEF intensity at the peak position (see Fig. S1). The relative intensity of the two Raman peaks was observed to remain constant as a function of both time and power densities for a given array of nanodiscs. This suggests that there is no change in the underlying plasmon resonance [7]. As a result, our experiments have focused on the 595 cm⁻¹ peak only, which allowed us to measure both Stokes and anti-Stokes scattering at the same time by centering the spectrometer at the laser wavelength. Fig. S1 shows an example of a SERRS spectrum used to determine the anti-Stokes to Stokes ratio.

* Eric.LeRu@vuw.ac.nz

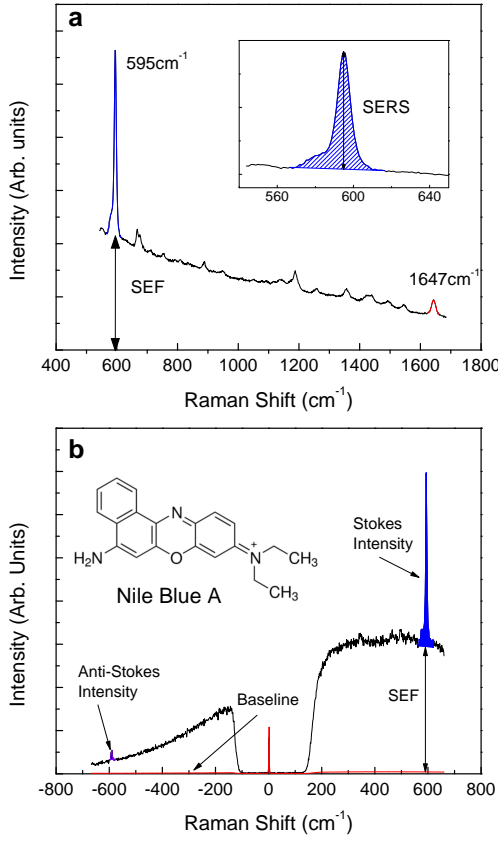


FIG. S1. **Spectrum of Nile Blue.** SERRS spectra of Nile Blue on the nanodiscs of array C at an excitation power of 3 kW cm^{-2} before photobleaching occurs. A Stokes Raman spectrum is shown in **a** and a spectrum centred at 0 cm^{-1} (for anti-Stokes to Stokes ratio) is shown in **b**. The SERRS intensities are calculated from the colored area of the peaks above the background. The SEF intensity used for calculating the total enhancement factor M_{Tot} is the intensity between the SERRS peak base and the baseline at the peak position.

S.II. GAUSSIAN BEAM EXCITATION

A. Theoretical description

As discussed in the text, the photobleaching decay curve can be strongly affected if a non-uniform excitation is used instead of a uniform excitation. This effect can be studied theoretically by considering the simple but relevant case of Gaussian beam excitation, for which we have:

$$S_L(\rho) = S_0 \exp\left(-2\frac{\rho^2}{w_0^2}\right), \quad (\text{S2})$$

which corresponds to a laser power $P_L = \pi w_0^2 S_0 / 2$. The fluorescence intensity (under normal conditions) is obtained by integrating Eq. 1 of the main text over the exciting area to give:

$$I_{\text{Fluo}}(t, P_L) = \mu_m Q^0 \sigma_{\text{Abs}}^0 P_L \frac{1 - \exp(-\gamma_B^0 S_0 t)}{\gamma_B^0 S_0 t} \quad (\text{S3})$$

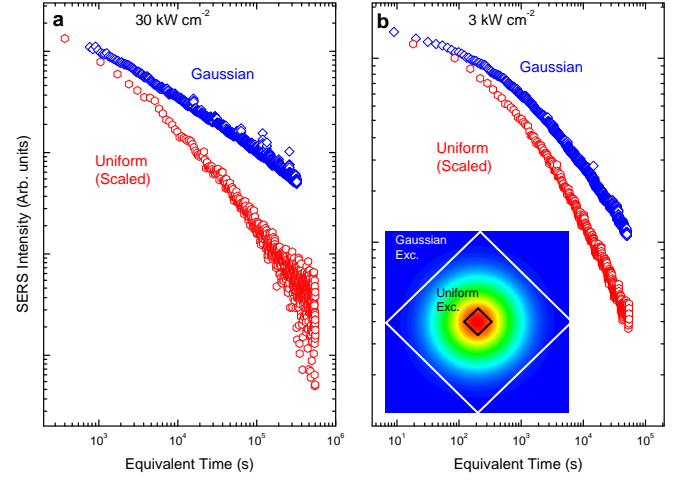


FIG. S2. **Effect of Gaussian beam excitation.** SERRS intensity profiles for Nile Blue measured on the nanodiscs of array C for illumination power densities (in the center of the excitation) of **a**, 30 kW cm^{-2} and **b**, 3 kW cm^{-2} for Gaussian excitation (open pinhole) and uniform excitation (small pinhole, see schematic in inset). Intensities are normalized to highlight the discrepancy in the photobleaching dynamics. Equivalent times are obtained from scaling to a reference power density of 50 W cm^{-2} using Eq. (11).

The decay is no longer mono-exponential despite the fact that all molecules have identical properties [8], and is in fact very different than the uniform excitation case as illustrated in Fig. 1b. On a log-log plot, the slope tends towards -1 irrespective of the actual laser power density. The SERS intensity can be obtained by integrating Eq. 8 over the exciting area to give:

$$\frac{I_{\text{SERS}}(t, S_L)}{\mu_m \sigma_{\text{Raman}}^0 P_L} = \int_{M_{\text{min}}}^{M_{\text{max}}} p(M) M^2 \frac{1 - \exp(-\alpha_B M S_0 t)}{\alpha_B M S_0 t} dM. \quad (\text{S4})$$

the effect of which is also illustrated in Fig. 1b.

B. Experimental evidence

For the reasons described above, we expect a significant change in the PB dynamics from uniform to non-uniform excitation. This is shown explicitly in the experimental results of Fig. S2 in which we compare the photobleaching curves for a Gaussian excitation (fully open confocal pinhole) with those obtained for uniform excitation (small pinhole). The measured intensity (at low power densities) is decreased by a factor of 10 in the latter case, because only the center area of the exciting beam is collected. In addition to this trivial intensity correction (which can be accounted for by considering normalized intensities), the measured PB curve is also strongly affected as shown in Fig. S2. The intensity for uniform excitation decreases much faster with time especially in

the case of the 30 kW cm^{-2} illumination power. The difference in measured intensities (normalized to low-power values) at longer time can be more than one order of magnitude. This is because a non-negligible part of the signal comes from those molecules in the tail of the illumination profile for a full Gaussian distribution, making it very difficult to fully photobleach the fluorophore population. The effect of the enhancement factor distribution then becomes convoluted with the distribution of power density associated with the non-uniformity of the excitation, making any quantitative analysis difficult. To avoid these issues, all experiments were carried out with a uniform excitation density as described in the Methods section.

S.III. TOTAL DECAY RATE ENHANCEMENT FACTOR M_{Tot}

In this work, we have assumed that the total decay rate enhancement factor M_{Tot} is approximately constant for all molecules adsorbed on to the gold surface. It was demonstrated in Ref. [9, 10] that for a common SERS probe (Crystal Violet), the ratio of Raman (SERRS) to fluorescence (SEF) was the same for all single-molecule SERRS events. Consequently, M_{Tot} was concluded to be the same for all molecules and dominated by non-radiative decay, which is in fact expected on theoretical grounds for fluorophores directly adsorbed on the metal surface and therefore with a large M_{Tot} ; a value of $M_{\text{Tot}} = 4 \times 10^5$ was also derived. In the system under study here, M_{Tot} can be measured in a similar fashion from the SERRS to SEF ratio. Although we are not in single-molecule SERRS conditions, the presence of photobleaching ensures that molecules with different EF are probed as a function of time. If M_{Tot} is not the same for all molecules because it is dominated by radiative decay, then the SERRS to SEF ratio should change dramatically with time. The SEF intensity was estimated by subtracting the baseline signal measured at a location on the substrate far from where the droplet was placed. M_{Tot} was then calculated by comparing the ratio of SERRS and SEF to the ratio of Raman to fluorescence cross-sections for Nile Blue in solution [2] (see Ref. [10] for details on estimating M_{Tot}). Fig. S3a shows the derived M_{Tot} as a function of time for incident power densities of 30 kW cm^{-2} , 18 kW cm^{-2} and 9 kW cm^{-2} on a flat gold film. In each of the three powers, M_{Tot} is constant with time at around 10^5 , which is of the same order as that measured in Ref. [10].

Additionally, M_{Tot} was measured on the nanodiscs of array C (see Fig. S3b). In this case, the baseline was estimated by completely photobleaching the observed area at 30 kW cm^{-2} (because the background signal from ITO is itself affected by the nanodiscs resonance [11]). We here observe a very strong increase in M_{Tot} for the lowest excitation powers. In this regime, the SERRS intensity hardly changes, so this dependence can be tracked down

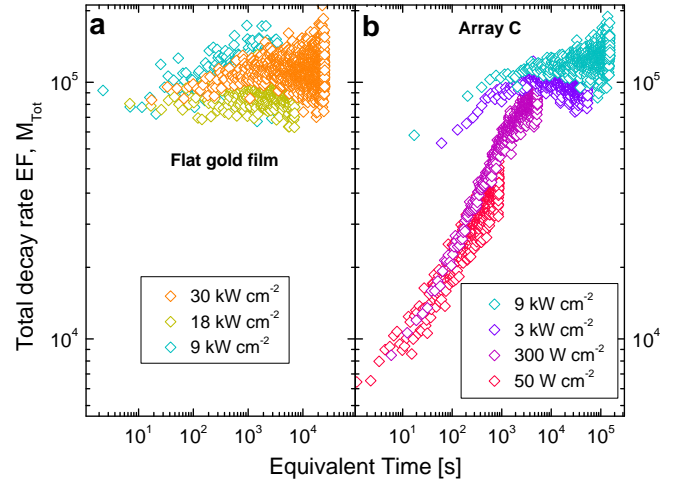


FIG. S3. **Total decay rate EF measurements.** Estimated M_{Tot} for Nile Blue as a function of time: **a**, on a flat gold substrate and incident power densities of $30, 18,$ and 9 kW cm^{-2} , and **b**, on the nanodiscs of array C with incident power densities of $9, 3, 0.3,$ and 0.05 kW cm^{-2} . Equivalent times are obtained from scaling to a reference power density of 50 W cm^{-2} using Eq. (11).

to an initial sharp decay of the SEF intensity, even for very low excitation powers. Because the SERRS intensity remains stable, this can be attributed to molecules with a very fast PB decay rate, but which do not contribute to the SERRS signal. This could either be due to Nile Blue molecules adsorbed on the ITO in between the nanodiscs or to extrinsic fluorescence by other contaminants. In any case, these only affect the initial SEF decay and not the SERRS signals. Once the source of this background fluorescence is photobleached, only the molecules adsorbed on gold remain allowing the measured M_{Tot} to converge to the same value of $\sim 10^5$ as observed on the flat gold film. We therefore conclude that all adsorbed molecules (those contributing to SERRS and to the PB decay curves) have a similar M_{Tot} of the order of 10^5 , as one can expect for fluorophores directly adsorbed on the metal surface where non-radiative decay dominates [9, 10].

S.IV. EXTRACTING THE EF DISTRIBUTION FROM THE PB DECAY CURVE

The PB decay curve $I_{\text{SERS}}(t)$ is related to the EF distribution $p(M)$ through Eq. 10 of the main text, which is repeated here for convenience:

$$I_{\text{SERS}}(t, S_L) = \mu_m \sigma_{\text{Raman}}^0 P_L \times \int_{M_{\text{min}}}^{M_{\text{max}}} p(M) M^2 \exp(-\alpha_B M S_L t) dM. \quad (\text{S5})$$

This relationship is complicated because of the integral

transform connecting the EF distribution and the time dependence, and one can expect that different EF distributions may lead to similar PB decays. This problem is similar to the inverse Laplace transform problem, which arises in various other fields involving time-dependent measurement with large distributions of decay rates, for example Nuclear Magnetic Resonance (NMR). Most fitting procedures face serious problems of ill-conditioning and unstable sensitivity to fitting parameters. Numerical methods like CONTIN [12] have nevertheless been developed and can be quite useful if used with care and if one assumes some pre-defined knowledge about the distribution of decay rates. To avoid these issues here, we have developed a similar stable fitting procedure adapted to our physical problem. The main steps are listed below:

- Because of the extreme nature of the EF probability distribution $p(M)$, which is expected to be long-tail and to cover many order of magnitudes for M [13, 14], we instead consider the random variable $K = \log_{10}(M)$ and try to find a fit to the function $f(K) = M^2 p(K) = 10^{2K} p(K)$. Note that $p(K) = p(M) M \ln(10)$. K no longer varies over several orders of magnitudes, and $f(K)$ can be expected to have a smooth dependence. Note also that the average SERS EF is simply obtained from $\langle M^2 \rangle = \int f(K) dK$.
- To avoid unstable fitting results, we rely only on linear least-square fits, which can be carried out efficiently and reproducibly using simple linear algebra. For this, we choose a minimum and maximum enhancement M_{\min} (or K_{\min}) and M_{\max} (or K_{\max}) and assume that $f(K)$ is a polynomial of order N in K over that range. K_{\min} , K_{\max} , and N are chosen and fixed before the fit, and the $N+1$ coefficients of the polynomial are the fitting parameters. The fit is then performed as a standard linear least-square problem.
- In order to set-up the linear least-squares problem, it is necessary to calculate integrals of the form:

$$\int_{K_{\min}}^{K_{\max}} K^n \exp(-\alpha_B 10^K S_L t) dK \quad (\text{S6})$$

for $0 \leq n \leq N$ and for all t -values in the fitted data. These integrals are computed numerically using a rectangular quadrature with 10^5 equally-spaced points

- From the fitted expression for $f(K)$, one can then derive $p(K) = f(K)10^{-2K}$, and $p(M)$ and all the other properties can be deduced from it. If the parameters K_{\min} , K_{\max} , and N are not adequate, then the fitted $f(K)$ will take non-physical negative values over the range of interest. K_{\min} , K_{\max} , and N should therefore be adjusted until a satisfactory fit is obtained. For this, it is recommended to set $N = 2$ first to find approximate values of K_{\min} ,

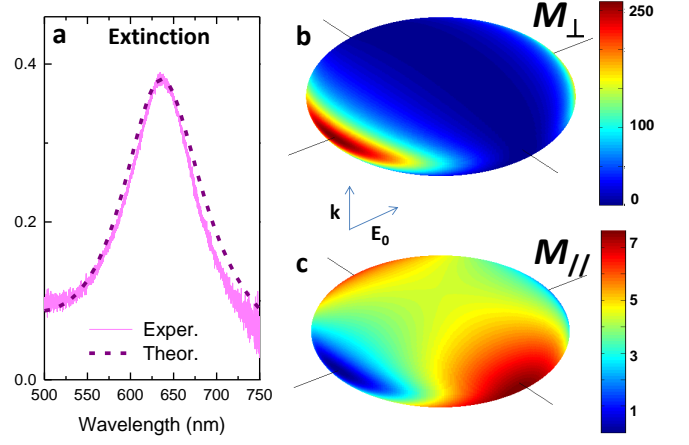


FIG. S4. **EM calculations.** Theoretical predictions for a gold nanodisc of array B, modelled as an oblate spheroid of long-axis 140 nm and short-axis 50 nm: **a**, Comparison of the predicted extinction spectrum with experimental results. **b**, distribution of the local-field intensity enhancement factor for the perpendicular component M_{\perp} at resonance ($\lambda = 633$ nm). **c**, Same for the parallel component M_{\parallel} .

K_{\max} , and then increase N to 3 or 4 if deemed necessary.

- It is important to understand that different solutions can result in a similar quality of fits, and the relevance of the results should be assessed carefully. From our experience, the value of M_{\max} is reliable within a factor of ~ 2 . There is a similar uncertainty on M_{\min} for a given set of experimental data, but its physical relevance is perhaps more questionable as M_{\min} depends strongly on the data at long times. Accessing long times is necessary to measure M_{\min} accurately, but it is a challenge experimentally. For a given system, the derived M_{\min} is therefore likely to vary with the maximum time measured. Because the average SERS EF $\langle M^2 \rangle$ depends strongly on M_{\min} in our system, it will also suffer from the same uncertainties.

S.V. ELECTROMAGNETIC MODELING OF GOLD NANODISCS

Electromagnetic (EM) calculations were carried out to predict the optical properties and enhancement factors of the gold nanodiscs. The exact predictions depend strongly on the details of the geometry (such as roughness and sharpness/roundedness of the edges), which are difficult to determine accurately. With these caveats in mind, the aim here is therefore to provide a semi-quantitative description of the main features. To do so, we therefore chose a simplified description of an isolated gold nanodisc on ITO modelled as an oblate spheroid embedded in a

medium of effective dielectric constant (ϵ_M). The main advantage is that EM calculations on spheroidal particles can be carried out efficiently and accurately using the methods developed in Ref. [15]. The dimensions were set by the experimental measurements (SEM in Fig. 2 for long-axis) and height of 50 nm for short axis. The resulting geometry is shown in Fig. S4b-c for array B. $\epsilon_M = (1.2)^2$ was chosen to match the measured plasmon resonance wavelength at 635 nm. The predicted extinction spectrum for array B is compared in Fig. S4a to the experimental results. The predicted enhancement factor (as local field intensity enhancement M) distribution on the surface is shown in Fig. S4b-c for both perpendicular and parallel components. From these distributions, the following surface-averaged values are obtained:

$$\begin{aligned} \langle M_{\perp}^2 \rangle &= 4500 & \langle M_{\parallel}^2 \rangle &= 27 \\ \langle M_{\perp} \rangle &= 39 & \langle M_{\parallel} \rangle &= 4.9 \\ M_{\perp}^{\max} &= 260 & M_{\parallel}^{\max} &= 7.6 \end{aligned} \quad (\text{S7})$$

S.VI. EXTRACTING THE TEMPERATURE FROM THE ANTI-STOKES/STOKES RATIO

From the early time average of the anti-Stokes/Stokes ratio ρ , we can estimate the fluorophore temperature using the relation [16]:

$$\rho = \frac{I_{aS}}{I_S} = A \exp\left(-\frac{\hbar\omega_{\nu}}{k_B T}\right) \quad (\text{S8})$$

where A is the asymmetry factor between anti-Stokes and Stokes scattering (primarily as a result of the underlying LSP resonance), $\hbar\omega_{\nu}$ is the energy of the vibrational mode, and $k_B T$ is the thermal energy. By assuming that the value of ρ measured for the lowest incident powers correspond to room temperature (293 K), we can estimate A for each array and use this value to calculate the temperature at the higher incident powers from Eq. S8.

-
- [1] Grofcsik, A., Kubinyi, M., & Jones, W. J. Fluorescence decay dynamics of organic dye molecules in solution. *J. Mol. Struct.* **348**, 197–200 (1995).
- [2] Reigue, A., Auguie, B., Etchegoin, P. G., & Le Ru, E. C. CW measurements of resonance Raman profiles, line-widths, and cross-sections of fluorescent dyes: Application to Nile Blue A in water and ethanol. *J. Raman Spectrosc.* **44**, 573–581 (2013).
- [3] Asimov, M. M., Gavrilenko, V. N., & Rubinov, A. N. Laser photolysis of laser dyes and the influence of triplet quenchers. *J. Luminescence* **46**, 243–249 (1990).
- [4] Le Ru, E. C. & Etchegoin, P. G. *Principles of surface-enhanced Raman spectroscopy and related plasmonic effects*. Elsevier, Amsterdam, (2009).
- [5] Eggeling, C., Widengren, J., Rigler, R., & Seidel, C. A. M. Photobleaching of fluorescent dyes under conditions used for single-molecule detection: Evidence of two-step photolysis. *Anal. Chem.* **70**, 2651–2659 (1998).
- [6] Drexhage, K. H. Fluorescence efficiency of laser dyes. *J. Res. National Bureau of Standards* **80A**, 421–428 (1976).
- [7] Le Ru, E. C., Etchegoin, P. G., Grand, J., Félidj, N., Aubard, J., Lévi, G., Hohenau, A., & Krenn, J. R. Surface enhanced Raman spectroscopy on nanolithography-prepared substrates. *Cur. Appl. Phys.* **8**, 467–470 (2008).
- [8] Berglund, A. J. Nonexponential statistics of fluorescence photobleaching. *J. Chem. Phys.* **121**, 2899–2903 (2004).
- [9] Le Ru, E. C., Blackie, E., Meyer, M., & Etchegoin, P. G. Surface enhanced Raman scattering enhancement factors: A comprehensive study. *J. Phys. Chem. C* **111**, 13794–13803 (2007).
- [10] Galloway, C. M., Etchegoin, P. G., & Le Ru, E. C. Ultrafast nonradiative decay rates on metallic surfaces by comparing surface-enhanced Raman and fluorescence signals of single molecules. *Phys. Rev. Lett.* **103**, 063003 (2009).
- [11] Le Ru, E. C., Grand, J., Félidj, N., Aubard, J., Lévi, G., Hohenau, A., Krenn, J. R., Blackie, E., & Etchegoin, P. G. Spectral profile modifications in metal-enhanced fluorescence. In *Metal-Enhanced Fluorescence*, Geddes, G., editor, 25–65. Wiley, (2010).
- [12] Provencher, S. W. A constrained regularization method for inverting data represented by linear algebraic or integral equations. *Comput. Phys. Commun.* **27**, 213 (1982).
- [13] Le Ru, E. C., Etchegoin, P. G., & Meyer, M. Enhancement factor distribution around a single surface-enhanced Raman scattering hot spot and its relation to single molecule detection. *J. Chem. Phys.* **125**, 204701 (2006).
- [14] Le Ru, E. C. & Etchegoin, P. G. Phenomenological local field enhancement factor distributions around electromagnetic hot spots. *J. Chem. Phys.* **130**, 181101 (2009).
- [15] Somerville, W. R. C., Auguie, B., & Le Ru, E. C. A new numerically stable implementation of the T -matrix method for electromagnetic scattering by spheroidal particles. *J. Quant. Spectrosc. Rad. Transfer* **123**, 153–168 (2013).
- [16] Maher, R. C., Galloway, C. M., Le Ru, E. C., Cohen, L. F., & Etchegoin, P. G. Vibrational pumping in surface enhanced raman scattering (sers). *Chemical Society Reviews* **39**, 965–979 (2008).